

Route towards stable homochiral topological textures in *A*-type antiferromagnets

Jack Harrison¹, Hariom Jani², and Paolo G. Radaelli^{1,*}

¹*Clarendon Laboratory, Department of Physics, University of Oxford, Oxford OX1 3PU, United Kingdom*

²*Department of Physics, National University of Singapore, 117411 Singapore*

 (Received 30 November 2021; revised 26 April 2022; accepted 23 May 2022; published 28 June 2022)

Topologically protected whirling magnetic textures could emerge as data carriers in next-generation post-Moore computing. Such textures are abundantly observed in ferromagnets (FMs); however, their anti-ferromagnetic (AFM) counterparts are expected to be even more relevant for device applications, as they promise ultrafast, deflection-free dynamics while being robust against external fields. Unfortunately, such textures have remained elusive; hence identifying materials hosting them is key to developing this technology. Here, we present comprehensive micromagnetic and analytical models investigating topological textures in the broad material class of *A*-type antiferromagnets, specifically focusing on the prototypical case of α -Fe₂O₃—an emerging candidate for AFM spintronics. By exploiting a symmetry-breaking interfacial Dzyaloshinskii-Moriya interaction (iDMI), it is possible to stabilize a wide topological family, including AFM (anti)merons, bimerons, and the hitherto undiscovered AFM skyrmions. While iDMI enforces homochirality and improves the stability of these textures, the widely tunable anisotropy and exchange interactions enable precise control of their core dimensions. We then present a unifying framework to model the scaling of texture sizes based on a simple dimensional analysis. As the parameters required to host and tune homochiral AFM textures may be obtained by rational materials design of α -Fe₂O₃, it could emerge as a promising platform to initiate AFM topological spintronics.

DOI: [10.1103/PhysRevB.105.224424](https://doi.org/10.1103/PhysRevB.105.224424)

I. INTRODUCTION

Topologically protected magnetic textures such as skyrmions and bimerons are emerging as prime information carriers in post-Moore memory and logic devices. Most research has focused on ferromagnetic (FM) materials, where examples of such textures are abundant [1–3], but deleterious effects intrinsic to FM topological textures, such as transverse deflection due to the skyrmion Hall effect, preclude their successful integration into devices. As a result, attention has shifted recently to antiferromagnets (AFMs), comprising oppositely aligned magnetic sublattices, as they are predicted to host ultrasmall skyrmions that are stable in the absence of applied fields and can be driven at very fast speeds [4–6]. However, no examples of isolated AFM skyrmions have yet been reported in the literature. Recently, there have been promising results in synthetic antiferromagnets [7,8]. While these materials solve the issue of lateral deflection, they may not be able to fully replicate the current-driven “relativistic” physics of natural AFMs due to their weaker interfacial exchange [9]. Hence discovering such topological textures in natural AFMs remains a key goal of the community.

Topological textures are typically stabilized by an inhomogeneous antisymmetric exchange term called the Dzyaloshinskii-Moriya interaction (DMI), with the material’s bulk DMI providing the required energy in many skyrmion-hosting systems [1]. Materials without bulk DMI can still host

stable chiral textures if an interfacial DMI (iDMI) is induced at the material surface [10], usually via an interaction with an overlayer or underlayer that has strong spin-orbit coupling [11]. The iDMI tends to favor Néel-type textures of a fixed chirality—an important feature since spin-torque-driven motion depends on chirality [12]. Homochiral topological AFM textures are expected to move consistently and reproducibly under the action of spin currents at speeds of up to a few km/s, making them promising as nonvolatile information carriers in spintronic devices [9,12–14].

Here, we focus on α -Fe₂O₃, which is a promising material candidate for AFM spintronics as it exhibits ultralow Gilbert damping and has exceptionally long and tunable spin diffusion [15,16], it shows a sizable spin-Hall magnetoresistance [17–19], and its AFM domain configurations can potentially be switched using pulsed currents through heavy-metal overlayers [20,21]. We previously reported the discovery of flat (anti)vortices in α -Fe₂O₃ thin films coupled to a ferromagnetic Co overlayer [22] and, more recently, of topological merons, antimeron, and bimerons in films with a Pt overlayer [23]. In the latter case, we were able to repeatedly nucleate and destroy these topological textures via thermally cycling through the spin-reorientation “Morin” transition, which is in some ways analogous to a Kibble-Zurek quench [24–26]. Since our observed textures were of both Bloch and Néel types and thus were not homochiral, we deduced that our samples had negligible iDMI. Understanding how to tune both the chirality and scale of AFM topological textures in the presence of iDMI is crucial for spintronics applications such as AFM topological racetracks.

*p.g.radaelli@physics.ox.ac.uk

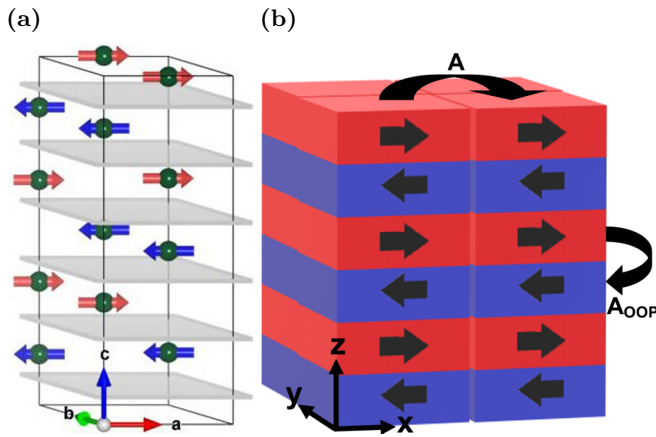


FIG. 1. (a) The crystal and magnetic structures of AFM α -Fe₂O₃, showing a sequence of antiparallel FM layers that we model in our simulations. The light red and dark blue arrows show the orientation of the magnetic moments in the two sublattices above T_M . The gray planes separate the two sublattices and host the O atoms. (b) The simulation configuration, where cells belonging to the two antiparallel sublattices are shown in red and blue and the arrows show the magnetic moment orientation in a given cell for $T > T_M$. The curved arrows show the AFM coupling between adjacent layers (A_{OOP}) and the FM coupling between cells in the same layer (A).

α -Fe₂O₃ crystallizes in the corundum structure (space group $R\bar{3}c$) and is an antiferromagnet with a relatively high Néel temperature (≈ 960 K) [27]. The magnetic moments in the antiferromagnetic phase stack with adjacent moments antiparallel along the c axis, such that moments in each a - b plane are ferromagnetically coupled [28]; see Fig. 1(a). This spin arrangement is generally known as A type of the classic field of perovskite magnetism, and we will use this terminology herein. α -Fe₂O₃ also hosts the Morin transition [29] at $T_M \approx 260$ K in bulk samples, where the anisotropy of the Fe³⁺ ions flips from being a - b easy plane for $T > T_M$ to easy axis along the c axis for $T < T_M$ due to a competition between on-site and dipolar anisotropies [30–33]. The resulting net anisotropy is strongly temperature dependent and changes sign at T_M . Consequently, both easy-plane and easy-axis domain morphologies can easily be studied via *in situ* temperature variations [17,22,23,33].

In this paper, we present our micromagnetic model for A -type antiferromagnets and confirm its validity through analytical calculations. We use this model to explore the effects of iDMI on a wide family of topological textures in the easy-plane and easy-axis phases of α -Fe₂O₃ by analytical calculations and micromagnetic simulations. We find that such textures become homochiral, making them ideal for spintronics applications where they can potentially be moved at ultrafast speeds via spin-orbit torques [14]. Moreover, their stability and size can be carefully controlled as a function of the material parameters to achieve the requirements for applications. A key prediction of this paper is that *antiferromagnetic skyrmions* should be stable in this system below the Morin transition for a wide range of physically realistic material parameters, which can be precisely engineered both during growth and *in situ*, making this an exciting and promising platform for their experimental discovery.

II. MICROMAGNETIC MODEL

A. General approach for A -type antiferromagnets

The application of micromagnetic modeling techniques and code such as MUMAX3 [34] to ferromagnetic bulk, films, and multilayers is extremely well documented. While some applications to antiferromagnets can also be found in the literature [35,36], it is not immediately obvious that these techniques can be applied to all antiferromagnets. Generally, one considers the micromagnetic scale to be much larger than the atomic scale, so that various magnetic interactions (exchange, anisotropy, and dipolar) can be replaced by their continuum counterparts. This assumption does not hold for an antiferromagnet, since the magnetization changes sign within every unit cell. In the case of A -type antiferromagnets such as α -Fe₂O₃ the situation is somewhat simpler, since these materials consist of ferromagnetic layers stacked in an antiparallel manner along an axis.

Here, we choose to model a generic A -type antiferromagnet as a set of layers stacked along the z axis of our simulation space [Fig. 1(b)]. We consider the magnetic moments to be antiferromagnetically coupled along the z axis and ferromagnetically coupled in the x - y plane. Akin to previous models of synthetic antiferromagnets [7,8], here the micromagnetic cell in the x - y plane is chosen to be much larger than the lattice parameter a , whereas its size along the z axis corresponds to the spacing of the ferromagnetic sublayers ($1/6$ of the lattice parameter c). The key energy terms are the exchange, anisotropy, dipolar, and interfacial Dzyaloshinskii-Moriya interactions, whose forms are given in Appendix A. Accounting for all of these energy terms accurately makes our model both general and widely applicable, allowing it to be extended to include additional energy terms and potentially leading to a variety of further studies of A -type AFMs.

Our approach differs from previous micromagnetic models of antiferromagnets [35,36], since here the spatial separation of the layers along the z axis has a physical meaning and we treat the dipolar fields organically rather than neglecting them entirely. The dipolar fields require special attention as they are typically long-range interactions, whereas all the other terms are short-range interactions between adjacent moments and are subsumed into scale-independent macroscopic parameters (see Appendix B). In essence, whereas the dipolar interaction decreases very rapidly at macroscopic distances, as expected for an antiferromagnet, its short-range component results in an in-plane (IP) anisotropy, so that the effective anisotropy of an A -type antiferromagnet, K_{eff} , is the sum of a dipolar component K_{dip} and of an on-site component K_{os} (if any exists). This is entirely physical, and the fine balance of K_{os} and K_{dip} is indeed the origin of the Morin transition in α -Fe₂O₃ [32]. While this accounts for the largest component of the dipolar fields, there may also be some small effects due to stray fields at the uncompensated surface layers, and any such effects will be included in our simulations.

It should be noted that our model has a number of limitations applying to all A -type antiferromagnets. Firstly, as already mentioned, the large antiferromagnetic exchange interaction along the z axis ensures that spins in adjacent layers are antiparallel. Therefore no variations in textures along the z axis can be studied as this model does not accurately

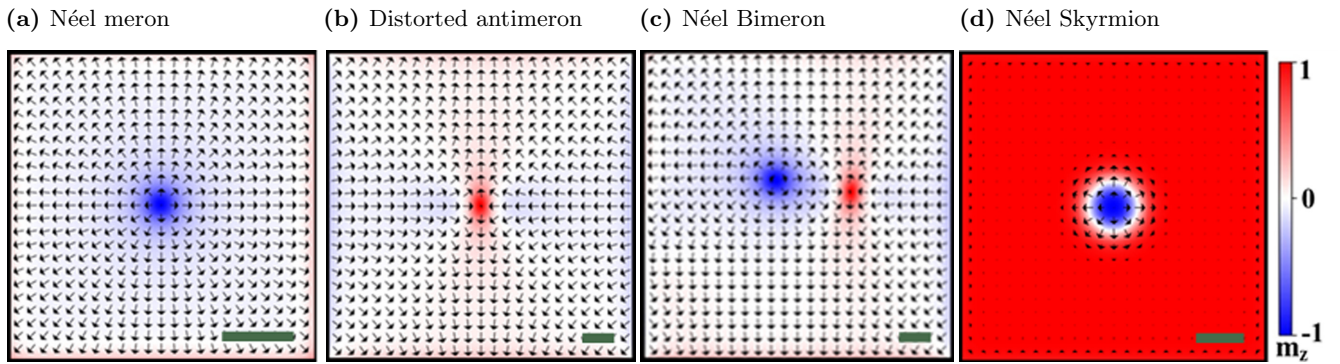


FIG. 2. (a)–(d) A gallery of topological textures in α - Fe_2O_3 , based on our micromagnetic simulations. In all cases only a single magnetic layer is shown. The black arrows represent the in-plane spin directions, and the color contrast corresponds to the z component of magnetization. The green scale bar in the bottom-right corner of each panel is 100 nm.

reproduce the atomic-scale interactions along this direction. By contrast, our approach is well suited to studying magnetic textures that are modulated in the x - y plane. In this paper we only consider very thin films, with total thickness much smaller than the characteristic length scale for magnetic variations along the z direction; hence this limitation will have a negligible effect on our simulations. Secondly, the dynamics at the nanometer length scale, primarily AFM spin waves, cannot be accurately simulated using this model [35], making it inappropriate for studying certain subsets of dynamical phenomena. Since our focus is the study of steady-state magnetization configurations via energy minimization, this drawback will also not affect our results.

There are a few additional caveats in the specific case of α - Fe_2O_3 . Firstly, this system has a weak bulk DMI, which causes a small canting of the two sublattices when $T > T_M$ leading to a small ferromagnetic component [30,37]. We neglect such a bulk DMI and its associated small canting throughout, as analytical calculations suggest that it cannot by itself stabilize IP-modulated topological textures. It should be noted that the small canting will become relevant if we want to extend the model to incorporate the effect of externally applied magnetic fields, which are not discussed here. Additionally, this system has a weak basal plane anisotropy due to its trigonal crystal structure, which favors the formation of a set of three 120° domains and their time-reversed counterparts when $T > T_M$; however, this anisotropy is orders of magnitude weaker than the uniaxial on-site anisotropy [31] and is therefore neglected here.

B. Micromagnetic simulations

Our simulations were performed using MUMAX3 [34,38,39], an open-source micromagnetics package utilizing finite-element simulations to model magnetic structures on the nanometer to micrometer length scales. This is ideal for topological textures, which tend to be around 100 nm or smaller [1,23]. The micromagnetic solver compares several energy terms as discussed in Sec. II A. For each simulation, the system was initialized with a certain configuration (meron, skyrmion, etc.), which was allowed to evolve using the conjugate gradient method [38] to minimize its energy. Given that we are considering *topological* structures, which are generally protected from collapsing due to a finite energy

barrier, the minimization procedure should only alter their size and geometry in a manner determined by the competition of the relevant energy terms, independent of the exact procedure used; for example, evolving the texture dynamically using the Landau-Lifshitz-Gilbert equation with large damping [40] should result in the same final topology. A texture whose final topology (after energy minimization) is identical to the initial topology is considered “stable” in these simulations, though it is generally metastable with respect to a uniform spin configuration. Minimized configurations for the key topological textures studied here can be found in Fig. 2.

The simulation is split into cuboid cells, each assigned a magnetic moment corresponding to the sublattice magnetization that is constant in each cell. Full details of the simulation parameters used are given in Appendix B. The demagnetizing field is calculated automatically in the software by convolving the magnetization field with the demagnetizing kernel [34], resulting in a demagnetization contribution to the total energy. In all our simulations this results in an effective easy-plane anisotropy of strength $K_{\text{dip}} \approx 530 \text{ kJ/m}^3$ perpendicular to the z axis, consistent with our discussion of the dipolar fields in Sec. II A. By applying an additional uniaxial on-site anisotropy of strength K_{os} along the z axis, we can simulate a Morin-like transition by varying K_{os} around K_{dip} . The effective anisotropy constant is given by $K_{\text{eff}} = K_{\text{os}} - K_{\text{dip}}$ and can switch sign from positive to negative, corresponding to out-of-plane (OOP) or IP orientations below or above the Morin transition, respectively. Performing a set of simulations without the demagnetizing fields and a readjusted anisotropy constant instead ($K_{\text{dip}} = 0, K_{\text{eff}} = K_{\text{os}}$) resulted in identical scaling of topological textures (see Sec. S3 of the Supplemental Material [41]). This suggests that any other effects of the demagnetizing fields are negligible when studying the static properties of topological textures. In our simulations, we also apply an iDMI of strength D (in the range ≈ 0.5 – 3 mJ/m^2) only to the topmost layer, thereby simulating a symmetry-broken magnetic surface hosting an interfacial antisymmetric exchange [11].

III. ANALYTICAL CALCULATIONS

Extensive analytical work has been performed to understand the shape and size scaling of skyrmions [5,6,42–

44]. Other topological textures, such as merons [45–47] and bimerons [14,48–51], have also been receiving attention recently. Complicated winding textures such as these are difficult to study analytically, especially when their functional forms are not known exactly. One possible simplification is to impose a particular functional form for the texture, usually called an “ansatz.” This often makes the problem solvable analytically, yielding an exact scaling that can be usefully compared with more realistic simulations. We calculated the exchange, anisotropy, and iDMI energy for a linear (anti)meron ansatz (see Appendix C) in order to derive the associated texture sizes and directly compare them with our micromagnetic simulations. The main purpose of this exercise is to provide a means of verifying our micromagnetic model, as well as to understand how the various textures scale with the material parameters.

Our approach here is analogous to calculations we have performed previously [23,52] but with the addition of the iDMI energy [10]. As discussed above, the dipolar field acts as an effective IP anisotropy to first order; therefore this was not included directly in our analytical calculations but rather rolled into the anisotropy. Merons are similar to flat vortices, but with an OOP core that results in a topological charge. For such textures, the effect of the iDMI is relatively straightforward, since it tends to stabilize circular homochiral textures of the Néel type. Using a linear meron ansatz, the analytical

expression for the meron radius R is (Appendix C 1)

$$R = l_w(\kappa + \sqrt{\kappa^2 + 1}) = \frac{3}{4}F, \quad (1)$$

where the final term in the above equation relates the meron “radius” R , which is the only free parameter of this specific ansatz, to the full width at half maximum (FWHM) F of the texture, which can be determined from the simulations. In Eq. (1), the characteristic length scale is $l_w = \eta\sqrt{A/|K_{\text{eff}}|}$, and we have introduced the dimensionless parameter $\kappa = \kappa_0 D_{\text{eff}}/\sqrt{A|K_{\text{eff}}|}$, which describes how strongly the iDMI energy affects the textures relative to the exchange and anisotropy. $D_{\text{eff}} = D/N$ is the rescaled iDMI parameter, where N is the total number of layers in our model system. Clearly, $R \rightarrow l_w$ in the limit $D_{\text{eff}} \rightarrow 0$. η and κ_0 are ansatz-dependent numerical constants; their values for a linear meron are derived in Appendix C 1.

By contrast, the situation for *antimerons* is more complex, since they are composed of sectors of alternating chirality. In the presence of iDMI the energetically favored Néel sectors contract, as the iDMI energy prefers tight spirals, resulting in an elongated (elliptical) antimeron. There are two key parameters that can be extracted by minimizing the antimeron energy (see Sec. S1 of the Supplemental Material [41]), namely, the radius R and distortion parameter λ , giving

$$R = l_w \left[\frac{1}{2}\kappa \left(\lambda - \frac{1}{\lambda} \right) + \sqrt{\frac{1}{4}\kappa^2 \left(\lambda - \frac{1}{\lambda} \right)^2 + \frac{1}{2} \left(\lambda^2 + \frac{1}{\lambda^2} \right)} \right] = \frac{3}{4} \sqrt{F_{\text{long}} F_{\text{short}}}, \quad (2)$$

$$\lambda = \frac{\kappa R}{2l_w [C + \ln(\frac{R_d}{R})]} + \sqrt{1 + \left\{ \frac{\kappa R}{2l_w [C + \ln(\frac{R_d}{R})]} \right\}^2} = \sqrt{\frac{F_{\text{long}}}{F_{\text{short}}}}, \quad (3)$$

where l_w , κ , η , and κ_0 are defined in the same way as for a meron. $C \approx 2$ is a numerical integration constant. Here, F_{long} and F_{short} correspond to the FWHM along the long and short axes of the antimeron, respectively. In our calculation, we confined the antimeron to a region of radius R_d , representing a cutoff on the effect of the antimeron distortion, which would otherwise extend to infinity as a con-

sequence of the analytical approach. These equations have an exact, albeit complicated, solution for R and λ for general κ and l_w if R_d is given; therefore we solve Eqs. (2) and (3) iteratively for given A , K_{eff} , and D . The results are convergent for all parameter values relevant here, given a reasonable initial guess of λ (see Sec. S1 of the Supplemental Material [41]).

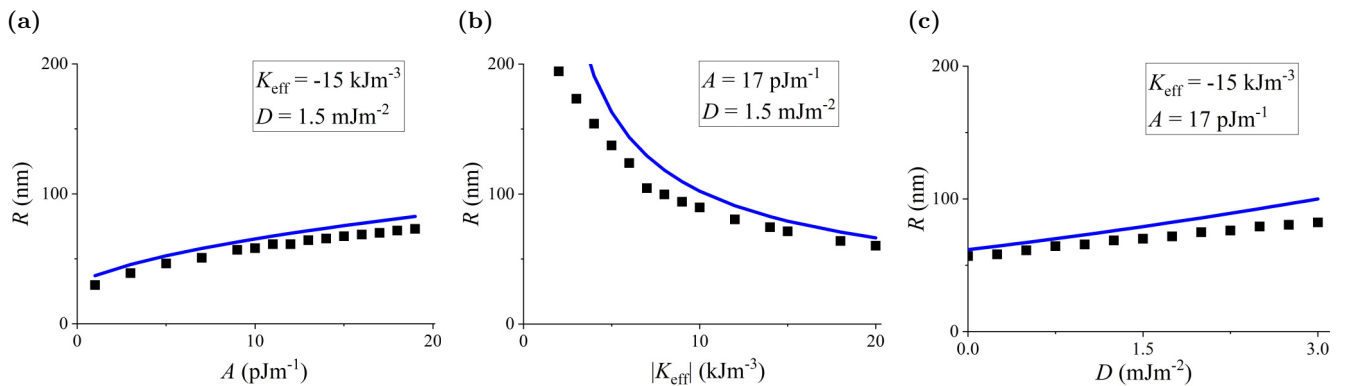


FIG. 3. Radius R of meron textures, based on micromagnetic simulations (black squares) and analytical calculations (blue curves). The iDMI was included in all cases. A , $|K_{\text{eff}}|$, and D were varied in (a), (b), and (c), respectively, with the rest of the parameters kept constant.

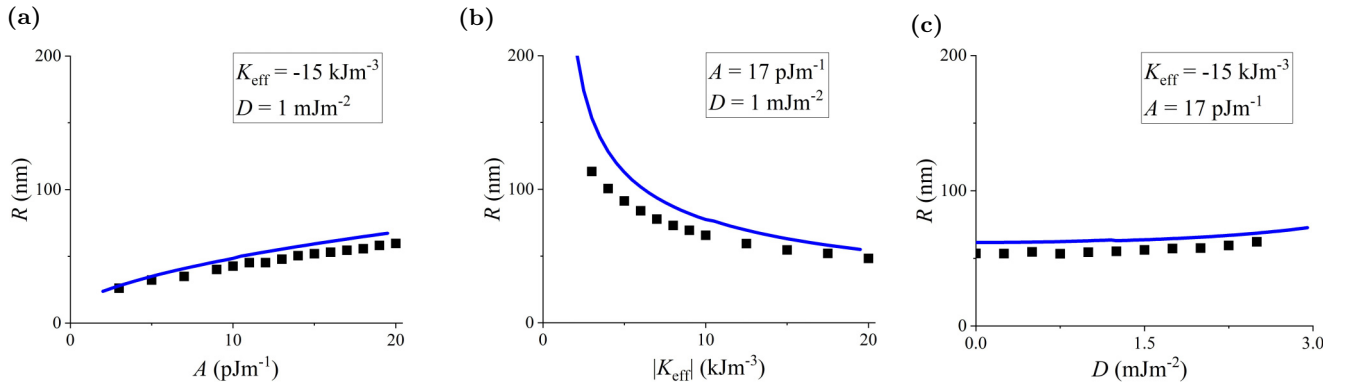


FIG. 4. Radius R of *antimeron textures*, based on micromagnetic simulations (black squares) and analytical calculations (blue curves). The iDMI was included in all cases. A , $|K_{\text{eff}}|$, and D were varied in (a), (b), and (c), respectively, with the rest of the parameters kept constant.

IV. SIMPLE EASY-PLANE TOPOLOGICAL TEXTURES

A. Merons

As merons require easy-plane anisotropy and therefore are observed in $\alpha\text{-Fe}_2\text{O}_3$ for $T > T_M$ [23], we use values of K_{Os} such that $K_{\text{eff}} < 0$. We performed micromagnetic simulations of isolated merons using our model for the case of zero iDMI as a consistency check (see Sec. S3 of the Supplemental Material [41]). To study the effects of iDMI, we also performed a set of meron simulations with nonzero D and compared their sizes with the analytical expression in Eq. (1) [Figs. 2(a) and 3]. As expected, the presence of iDMI enforces a specific chirality, making all such merons Néel type. The scaling with A and $|K_{\text{eff}}|$ is, to lowest order, similar to that found for the case of a meron without iDMI [23], and the functional form that we determined analytically provides a satisfactory approximation to the simulations. The key trends are that the meron radius increases if we increase the strength of the exchange or DMI, while decreasing rapidly as we increase the strength of the IP anisotropy. There appears to be some difference in the actual FWHM values when comparing the simulations and analytics, which is not surprising, since the numerical prefactors contained in l_w and κ are strongly affected by the choice of the ansatz; calculations for a different ansatz would give different numerical factors [52]. The qualitative agreement between our computational model and analytical calculations demonstrates that our approach is both reasonable and internally consistent.

B. Antimerons

We performed simulations of isolated antimerons with iDMI and found that they were indeed stable and distorted [Fig. 2(b)]. We have therefore calculated the effective radius R of the simulated antimeron using Eq. (2) and compared it with the analytical values (Fig. 4). The analytical curve was calculated iteratively using Eqs. (2) and (3) for the same set of values of A , $|K_{\text{eff}}|$, and D used in the simulations and with the cutoff radius R_d set to the simulation radius. It should be noted that varying R_d , even by an order of magnitude, has a minimal effect on the resulting analytical radius.

Here, the antimeron radius increases with increasing exchange strength, is roughly independent of the iDMI strength, and decreases rapidly as the IP anisotropy increases. The

scaling of antimerons as a function of A , $|K_{\text{eff}}|$, and D is qualitatively similar to that of merons; however, there is again a slight difference between the analytical and simulated radius due to the ansatz choice. While the scalings of the distortion with the various energy terms match qualitatively, the analytically calculated value of the distortion parameter λ is consistently smaller compared with the value extracted from the simulations, by a factor of ~ 3 – 5 ; see Sec. S4 of the Supplemental Material [41]. Despite these caveats, the scaling behaviors of R in both the analytical and simulated antimerons match reasonably well, and they both predict that antimerons should distort in the presence of iDMI.

V. COMPOUND EASY-PLANE TOPOLOGICAL TEXTURES

A. Bimerons and topologically trivial meron pairs

In our previous study [23] we reported the observation of meron-antimeron pairs in $\alpha\text{-Fe}_2\text{O}_3$, which could be either topologically trivial meron pairs (TTMPs) or topologically nontrivial bimerons, depending on whether the core polarization of the constituent (anti)merons are aligned or antialigned, respectively [Fig. 2(c)]. Since constructing an analytical model for such compound objects using a realistic ansatz is difficult, we investigated their properties using micromagnetic simulations. We initialize a meron-antimeron pair in the system that is either a TTMP or a bimeron in the IP state ($K_{\text{eff}} < 0$) by placing a meron in one-half of the simulation and an antimeron in the other half with the desired core polarities. We then allow them to relax naturally into their preferred configurations. We observe that neither TTMPs nor bimerons are stable in the absence of iDMI. The observed collapse indicates that the competition between exchange and anisotropy energies alone is insufficient to stabilize such textures, despite the supposed topological protection of bimerons.

If we introduce iDMI into the system, bimerons become stable over a very wide parameter range, even when initialized at very close distances (≤ 150 nm; Fig. 5), whereas TTMPs are only stable if they start a long way apart, at which point they could be considered as isolated merons and antimerons. This makes phenomenological sense as bimerons have a net topological charge and therefore should be prevented from collapsing due to a finite energy barrier afforded by iDMI, which is expected to be absent in TTMPs. For small values

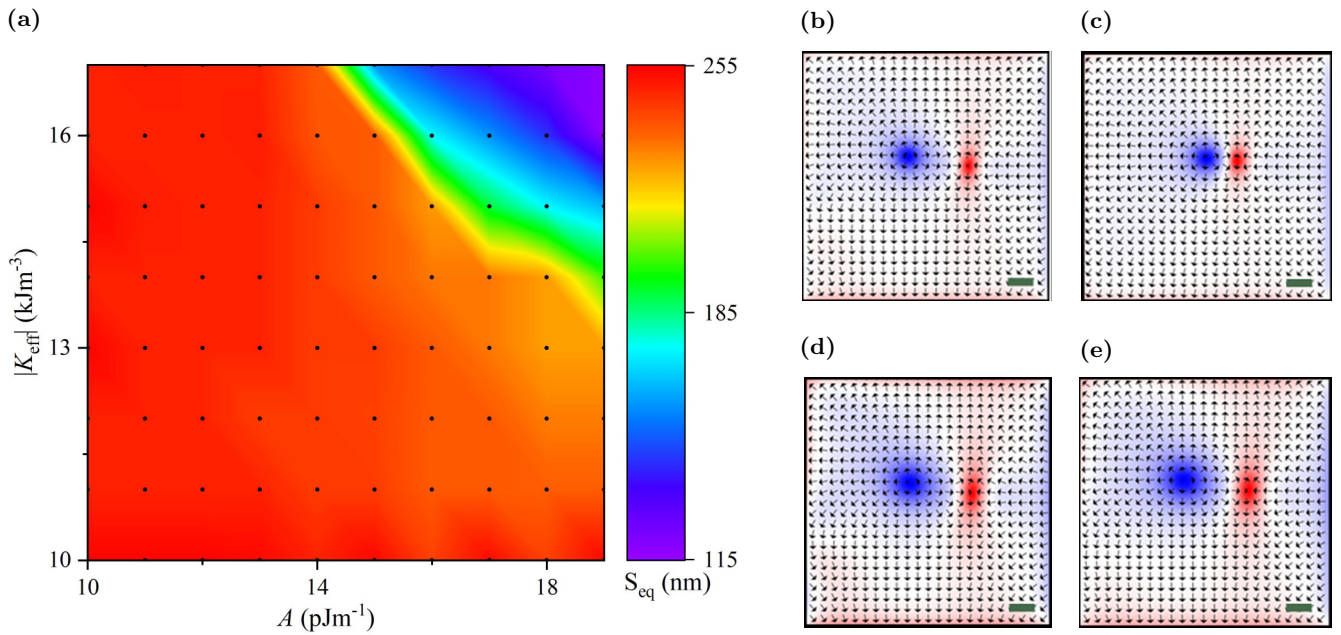


FIG. 5. (a) Relaxed Néel bimeron intercore distance s_{eq} as a function of A and K_{eff} for $D = 2$ mJ/m². The simulation points are given by solid black circles. (b)–(e) Snapshots of the relaxed configuration in one of the layers for several points in the diagram, where the arrows represent the IP spin direction and the color contrast represents the z component of the magnetization as in Fig. 2. The green scale bar in the bottom-right corner of (b)–(e) is 100 nm. The images correspond to the following values: (b) $A = 14$ pJ/m, $K_{\text{eff}} = -17$ kJ/m³; (c) $A = 19$ pJ/m, $K_{\text{eff}} = -17$ kJ/m³; (d) $A = 14$ pJ/m, $K_{\text{eff}} = -10$ kJ/m³; and (e) $A = 19$ pJ/m, $K_{\text{eff}} = -10$ kJ/m³.

of A , the intercore distance remains large for all values of $|K_{\text{eff}}|$, whereas for larger values of A the intercore distance is highly tunable as a function of $|K_{\text{eff}}|$. Fundamentally, the size scaling for tightly bound bimerons can depend only on the dimensionless parameter κ and the length scale l_w , as introduced in Secs. III and VII. It should be noted that the antimeron component is distorted, causing the bimeron to lose circular symmetry [49].

While our simulations do not address the question of the barrier height directly, we can make some general observations. Assuming a quadratic potential around the equilibrium intercore (anti)meron separation s_{eq} , we can approximate the energy of the bimeron (up to quadratic order) as

$$E = \alpha + \beta s + \gamma s^2, \quad (4)$$

where α , $\beta < 0$, and $\gamma > 0$ are unknown phenomenological parameters that enforce a positive-curvature quadratic with $s > 0$. For a certain simple ansatz, such as the linear bimeron (see Appendix C 2), we can identify these three parameters with the micromagnetic parameters A , D_{eff} , and K_{eff} , respectively, up to some numerical factors. As a result, we can derive the equilibrium separation $s_{\text{eq}} = -\beta/(2\gamma) \propto D_{\text{eff}}/K_{\text{eff}}$ and the barrier height $\Delta = E(0) - E(s) = \beta^2/(4\gamma) = -0.5\beta s_{\text{eq}} \propto D_{\text{eff}}^2/K_{\text{eff}}$. It is clear from our simulation data that the exchange strength A does play a role in determining the bimeron size and therefore likely the barrier height, which is not accounted for in the linear bimeron solution, meaning that the relationship between the phenomenological and micromagnetic parameters is in reality more complicated. Regardless of the exact expression, these considerations indicate that the route towards experimentally realizing closely bound, stable bimerons is to maximize Δ and minimize s_{eq} at the same time, which requires increasing both D and K_{eff} .

B. Comparison with experiments

When comparing the present results with our recent experiments [23], we are faced with an apparent contradiction. Experimentally, we observed that merons had varied chirality, which seems to rule out the presence of significant iDMI; however, we also observed meron-antimeron pairs that appeared to be quite robust, demonstrating that their lifetimes must be extremely long and implying that the associated energy barrier to annihilation is large. In our simulations, this is only possible in the presence of iDMI. These contrasting observations suggest that an alternative mechanism not accounted for in our micromagnetic model might be responsible in the real system for the apparent stability of these pairs. In terms of the phenomenological model discussed earlier, this means that some additional energy term, other than the exchange, anisotropy, and iDMI considered throughout, likely contributes to the barrier height Δ . An alternative explanation is that the potential landscape is locally flat, allowing both bimerons and TTMPs to be trapped by local defects even in the absence of an “intrinsic” potential barrier. This implies that our phenomenological model would need to go beyond the quadratic approximation, such that the intercore force need not always increase with distance.

For practical implementation of homochiral bimerons in α -Fe₂O₃-based racetrack applications, we cannot rely on defects or other local pinning mechanisms to achieve stability because the bimerons must be *mobile*. Therefore we require bimerons to exist in a local energy minimum at a small intercore distance s_{eq} between the meron and antimeron as well as a large energy barrier Δ to prevent bimeron annihilation. Our simulations clearly imply that we should be able to engineer the material parameters in such a way as to achieve this goal

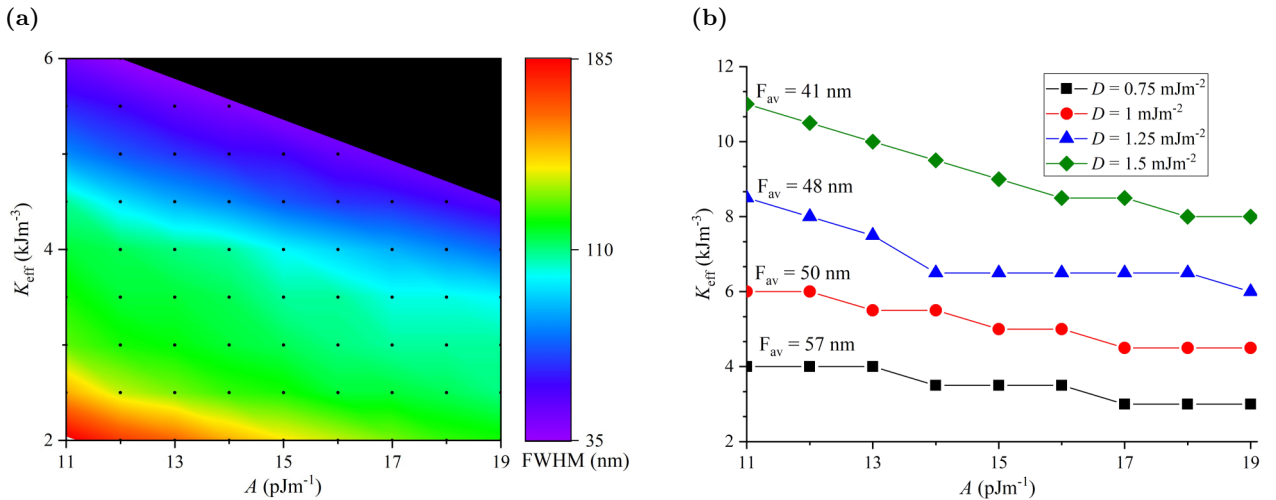


FIG. 6. (a) Néel skyrmion stability window as a function of A and K_{eff} for $D = 1 \text{ mJ/m}^2$. The color scale represents the relaxed FWHM of the skyrmions, and the black area shows the region where the skyrmion was found to radially collapse and therefore was unstable. The A and K_{eff} values for which simulations were performed are shown by solid black circles. (b) K_{eff} -vs- A curves at constant skyrmion radius, calculated for the smallest size for which a skyrmion can be stabilized in our simulations (given by the F_{av} value next to each curve). Symbols and colors correspond to different iDMI strengths.

and that this can only be achieved by topologically protected bimerons (rather than TTMPs) in the presence of a reasonably strong iDMI.

VI. EASY-AXIS TOPOLOGICAL TEXTURES (SKYRMIONS)

Here, we discuss the possibility to stabilize *antiferromagnetic skyrmions* in $\alpha\text{-Fe}_2\text{O}_3$. These have not been observed experimentally thus far but, as we demonstrate here, are stable in our simulations over a wide range of material parameter values. In $\alpha\text{-Fe}_2\text{O}_3$, a skyrmion can only exist in the easy-axis phase ($T < T_M$); their experimental discovery would significantly increase the flexibility of the system, as topological textures have previously only been observed for $T > T_M$ [23]. It is worth pointing out that the Morin temperature can be raised well above room temperature by chemical doping [23,33], allowing practical exploitation of such skyrmions. As in the case of bimerons and of skyrmions in other systems without bulk DMI, it is necessary to have a sizable iDMI to stabilize these textures. We therefore initialized a Néel skyrmion with $K_{\text{eff}} > 0$ (i.e., an easy-axis anisotropy along z) in the presence of an iDMI. An example of such a skyrmion can be seen in Fig. 2(d), and the full stability window for a range of A , K_{eff} , and D values is shown in Figs. 6(a) and 6(b). For a wide range of micromagnetic parameters, the skyrmion remained stable and either grew or shrank to an equilibrium size. As expected, these skyrmions are always Néel type, which is favored by the iDMI. Consequently, when we initialized a Bloch-type skyrmion, the spins globally rotated into the Néel configuration.

We can also study the tuning of physical parameters (A and K_{eff}) required to minimize the skyrmion size in our system for a given D [see Fig. 6(b)]. The data in Fig. 6 point towards a threshold radius, below which the skyrmions spontaneously evaporate via radial collapse [53,54]. This is likely due to a

breakdown in the micromagnetic regime (where the finite cell size is on the same order as the length scale of variations). Hence the sizes shown in Fig. 6(b) in fact represent an upper limit to the minimum achievable skyrmion size in this material system, and in reality, smaller skyrmions that cannot be reasonably simulated using micromagnetics may also be stable. This shows the potential to generate ultrasmall antiferromagnetic skyrmions for practical applications in $\alpha\text{-Fe}_2\text{O}_3$.

As can be seen in Fig. 6(b), increasing the iDMI strength D or decreasing the exchange coupling A increases the maximum anisotropy K_{eff} for which skyrmions are stable. Given the nature of the Morin transition, increasing the strength of K_{eff} for $T < T_M$ at fixed A corresponds to reducing the temperature of the system. Therefore, to maximize the thermal stability window for skyrmions in $\alpha\text{-Fe}_2\text{O}_3$, we need to engineer films with small A and large D . Based on our previous data, this thermal stability window is already of the order of 20 K for the smallest value of D considered here (see Appendix B). This is important to understand, as applications for AFM skyrmions require a large window of thermal stability.

To conclude this section, we emphasize a key prediction of our micromagnetic model: The long-sought-after *antiferromagnetic skyrmion* should be stable and therefore observable in $\alpha\text{-Fe}_2\text{O}_3$ and potentially other A -type antiferromagnets. While the possibility of stabilizing skyrmions in easy-axis AFMs with iDMI has been studied previously, we push this further by proposing a specific system where the material parameters are appropriate, or can be engineered to be appropriate in a well-understood manner, for their stabilization and experimental verification.

VII. PHENOMENOLOGICAL SCALING

Finally, we discuss the size scaling of various topological textures described herein and demonstrate that our micromagnetic simulations recreate the phenomenological scaling one

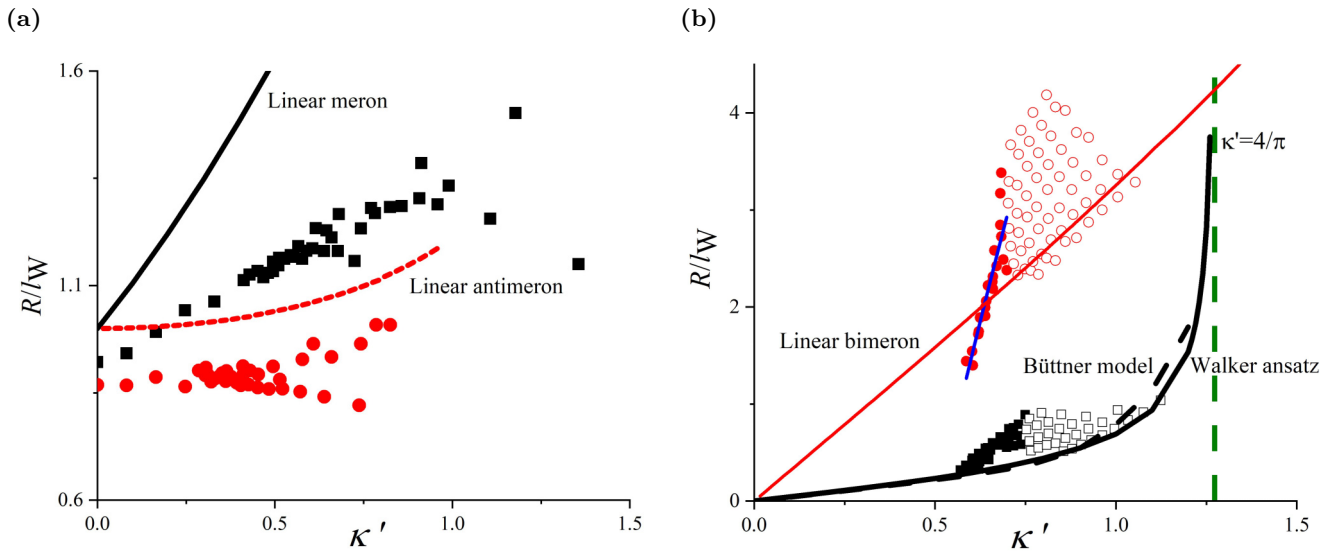


FIG. 7. (a) Rescaled radii of simulated merons (black squares) and antimerons (red circles) as a function of $\kappa' = D_{\text{eff}}/\sqrt{AK_{\text{eff}}}$ compared with the corresponding linear meron (antimeron) ansatz, Eq. (1) [Eq. (2)]. (b) Rescaled radii of skyrmions (black squares) and bimerons (red circles). In each case the solid symbols show the smaller textures in the approximately linear scaling regime, and open symbols show larger textures where the energy landscape is very flat. An analytical linear bimeron model and two different types of skyrmion ansatz [42,43] are shown for comparison. The blue line is a linear fit to the small radii bimerons. The vertical green dashed line shows the well-known upper stability threshold for skyrmions at $\kappa' = 4/\pi$, demonstrating that our skyrmions do not reach this threshold for any material parameters considered herein.

can expect from simple dimensional analysis. The three materials parameters in our simulations have dimensions $[A] = \text{J/m}$, $[K_{\text{eff}}] = \text{J/m}^3$, and $[D_{\text{eff}}] = \text{J/m}^2$. With these, we can form a *single* dimensionless parameter $\kappa' = D_{\text{eff}}/\sqrt{AK_{\text{eff}}}$ and a length scale $l_w = \sqrt{A/K_{\text{eff}}}$. All length scales in the problem must therefore be proportional to l_w multiplied by a dimensionless function of κ' ; this is consistent with our analytical calculations [Eqs. (1) and (2)]. Hence, if we were to divide all the relevant sizes of the textures, as extracted from our simulations, by l_w , we would expect the results to scale as a function of κ' only. This is demonstrated in Fig. 7, where the texture radii are rescaled by $l_w = \eta\sqrt{A/K_{\text{eff}}}$, which is the relevant length scale for the linear (anti)meron ansatz as discussed above (see Sec. III), and then plotted as a function of κ' . This analysis has two purposes: firstly, to compare the simulated textures with various analytical models presented here and other skyrmion models [42,43] in the literature and, secondly, to establish whether or not our simulations have reached equilibrium, which is a precondition for scaling.

Concerning the first point, for the (anti)meron textures [Fig. 7(a)] it is clear that our linear ansatz models reproduce the observed functional scaling to a good approximation, only differing by numerical factors of the order of 1, which is consistent with our discussions throughout. The same is not true for bimerons [Fig. 7(b)], which clearly display a different functional dependence from the linear approximation (see Sec. S2 of the Supplemental Material [41]), although the sizes are of the correct order of magnitude. We also report the scaling for our AFM skyrmions, which is in good agreement with established skyrmion models in the literature within the range of stability. A straightforward observation is that skyrmions are generally much smaller than bimerons in the whole range of parameters we explored, suggesting

that they might be more suitable textures for applications of A-type antiferromagnets. Additionally, while many analytical skyrmion models predict a stability threshold for larger κ' , they fail to predict the lower threshold for κ' . This is because these are all continuum models that do not account for the atomic nature of the system, which becomes important as the skyrmion approaches smaller length scales.

Turning to the second point, there is a clear distinction between smaller and larger skyrmions or bimerons; while smaller textures scale roughly linearly with κ' , larger textures do not obey any obvious scaling. This is likely because they have not reached their equilibrium radii due to the locally flat energy landscape about the equilibrium (which can be seen by studying the solutions in Ref. [42]). In this regime, a range of different sized textures are observed within the simulation tolerances for a given κ' . We remark that the textures we are interested in for applications, namely, those that are small, are also those that fortuitously obey the expected scaling law as a function of κ' . We also note that this spread of texture sizes for a given κ' is not necessarily just an artifact of the simulations, as local strain and thermal fluctuations could also lead to this effect in a real system and this will be most pronounced when the energy landscape is locally flat near the equilibrium.

VIII. SUMMARY

We have presented a comprehensive micromagnetic model for A-type antiferromagnets and applied it to the study of topological textures in $\alpha\text{-Fe}_2\text{O}_3$ with interfacial DMI. Firstly, we verified our model by comparing simulated Néel merons and distorted antimerons with corresponding analytical calculations. Given the simplicity of our analytical ansatz, the consistency between the simulated and analytical scalings of

these textures is remarkable. Then, we used our model to analyze the properties of Néel bimerons in the presence of iDMI and compared their stability and scaling behavior with those in our recent experiments. Finally, we demonstrated that α -Fe₂O₃ can also host the long-sought-after Néel *antiferromagnetic skyrmions* and discussed the requirements to experimentally stabilize and observe such textures. We emphasize that our results here demonstrate that a wide family of homochiral topological textures can be stabilized in both the IP phase and OOP phase of this material, making α -Fe₂O₃ an ideal platform for exploring beyond-Moore device architectures exploiting AFM topological textures.

ACKNOWLEDGMENTS

The work done at the University of Oxford was funded by EPSRC Grant No. EP/M2020517/1 (Quantum Materials Platform Grant). The work at the National University of Singapore was supported by the National Research Foundation under the Competitive Research Program (NRF-CRP15-2015-01). This work (J.H.) was supported by the EPSRC (GB) (DTP Grant No. 2285094).

APPENDIX A: ENERGY TERMS

For our models we include four energy terms in a continuous form, these being the exchange, uniaxial anisotropy, dipolar, and iDMI energies as follows:

$$E_{\text{Ex}} = \iiint A \left[\left(\frac{\partial \hat{\mathbf{m}}}{\partial x} \right)^2 + \left(\frac{\partial \hat{\mathbf{m}}}{\partial y} \right)^2 \right] d^3r, \quad (\text{A1})$$

$$E_{\text{An}} = \iiint -K_{\text{eff}} (\hat{\mathbf{u}} \cdot \hat{\mathbf{m}})^2 d^3r, \quad (\text{A2})$$

$$E_{\text{Dip}} = \iiint -\frac{1}{2} (\vec{\mu} \cdot \vec{h}) d^3r, \quad (\text{A3})$$

$$E_{\text{DMI}} = t \iint D \left(m_x \frac{\partial m_z}{\partial x} - m_z \frac{\partial m_x}{\partial x} + m_y \frac{\partial m_z}{\partial y} - m_z \frac{\partial m_y}{\partial y} \right) d^2r. \quad (\text{A4})$$

A , K_{eff} , and D are the exchange, uniaxial anisotropy, and iDMI constants, respectively. $\hat{\mathbf{m}}$ is the unit magnetization vector field of the sublattice, $\hat{\mathbf{u}}$ is the anisotropy axis, $\vec{\mu}$ is the local magnetic moment, \vec{h} is the local dipolar field, and t is the “effective range” of the iDMI (see below) [10,40]. The micromagnetic simulations utilize a discretized version of these equations [34,38,39]. In our model, an exchange interaction of the form in Eq. (A1) only applies to the ferromagnetic interactions between adjacent cells in the same layer (we recall that the interlayer exchange strictly enforces antiparallel alignment between adjacent layers in this model). Note that $K_{\text{eff}} > 0$ yields an easy axis parallel to $\hat{\mathbf{u}}$ whereas $K_{\text{eff}} < 0$ yields an easy plane perpendicular to $\hat{\mathbf{u}}$. Equation (A4) requires the iDMI energy to be uniform throughout a thickness t [10], which we assume to correspond to the thickness of a single AFM layer. This is different from the other three energy terms, which are volume integrals, whereas the iDMI

contribution comes from a surface integral. This implies no loss of generality, provided we assume that the textures are not modulated along \hat{z} .

APPENDIX B: MICROMAGNETIC PARAMETERS OF α -Fe₂O₃

In our simulations, the cell size along the z axis was fixed at 0.228 nm, corresponding to 1/6 of the unit cell and the spacing between AFM layers [27]. The simulation size and cell size were adjusted for each different texture type to ensure a good compromise between simulation time and texture scales in each case, given that the skyrmion and bimeron simulations took an order of magnitude longer than the (anti)meron simulations. In all cases, different cell dimensions and total simulation dimensions were checked and found to be consistent, and all satisfied the micromagnetic guideline of a maximum angle between adjacent moments of no more than 20° (in the x - y plane); hence the choices made throughout are purely a matter of convenience.

The sublattice saturation magnetization of α -Fe₂O₃ is 920 kA/m [27]. The IP exchange constant A in α -Fe₂O₃ (i.e., the ferromagnetic interaction between cells in the same layer) is around 14–17 pJ/m [23] depending on the exchange parameters used to calculate it [27,55], and this can be altered further via doping or strain [56,57], justifying the range of values $A = 10$ –20 pJ/m used here. The AFM coupling between adjacent layers was similarly calculated to be $A_{\text{OOP}} = -20.1$ pJ/m and is kept constant throughout. As the long-range dipolar fields are negligible, the corresponding z -axis magnetic exchange length $l_{\text{ex}} = \sqrt{2A/(\mu_0 m_s^2)}$ (where m_s is the weak canted ferromagnetic moment) will be much larger than the simulation size along z , so we expect negligible texture variation in this dimension (consistent with all our simulations). We have additionally confirmed that altering the cell size along z has no discernible effect on the textures, thereby further justifying our approach.

In α -Fe₂O₃, the effective anisotropy constant K_{eff} results from a competition of on-site and dipolar interactions [30–32], with the Morin transition T_{M} occurring when these two interactions balance. This competition can be tuned by strain, chemical doping, and reversible ionic control to alter T_{M} or destroy the transition altogether [31,33,57]. As both the on-site and dipolar anisotropies are temperature dependent, the value of K_{eff} varies systematically on either side of T_{M} , and these values can be calculated and directly compared with our simulation data. For example, using the representative values $A = 14$ pJ/m and $D = 0.75$ mJ/m², the maximum anisotropy value for which we observed stable skyrmions was $K_{\text{eff}} = 3.5$ kJ/m³ [see Fig. 6(b)]. Based on a thin film with $T_{\text{M}} = 240$ K, similar to that used in our previous experiments [23], this maximum anisotropy corresponds to a temperature of approximately 219 K, meaning that we estimate the skyrmion stability window to be on the order of 20 K below T_{M} , which is certainly a feasible range for practical observation of these textures. As we are not aware of any work studying or engineering possible iDMI strengths in α -Fe₂O₃ systems, we have used values of D throughout that are akin to those used in other theoretical studies [5,11,42] and to those found in

the large body of work on topological-texture-hosting Co-Pt heterostructures [58].

As briefly outlined in Sec. II A, the dipolar fields can be approximately decomposed into two parts: the short-range dipole interaction, which is generally taken to contribute to the anisotropy energy and is therefore not included in the model separately, and the long-range part, which is computed directly in the form of a demagnetization field [40]. In a natural collinear antiferromagnet, the net magnetization is zero, and so is the demagnetization field, but the short-range component of the dipolar interaction still contributes to the anisotropy. In our “model” *A*-type antiferromagnet, each magnetic cell has an exactly antiparallel counterpart in a vertically adjacent layer. Therefore the calculated demagnetization field has a quadrupolar character and decays very rapidly. Although there are no macroscopic demagnetization fields and there is no shape anisotropy, the short-range part of the quadrupolar interaction still generates an anisotropy, inducing a strong preference for the moments to lie in the *x*-*y* plane even when the on-site anisotropy energy density is set to zero. This situation is very similar to that of “real” α -Fe₂O₃, since the Morin transition occurs precisely when the easy-axis on-site anisotropy exactly balances the perpendicular easy-plane dipolar anisotropy. As our simulations use a cuboidal configuration rather than stacked honeycomb layers, we would not expect the dipolar anisotropy to be exactly the same as for the real material, but the order of magnitude should be correct. In fact, our calculated dipolar anisotropy is approximately 60% of the known value for α -Fe₂O₃. For now, we observe that our model *A*-type antiferromagnet provides a good physical account of the real material, provided that the dipolar anisotropy calculated by the micromagnetic code is properly taken into account.

APPENDIX C: ANALYTICAL CALCULATIONS

In polar coordinates, the linear (anti)meron ansatz for the unit magnetization vector $\hat{m} = (\sin \theta \cos(\phi + \xi), \pm \sin \theta \sin(\phi + \xi), \cos \theta)$ is

$$\theta(r) = \begin{cases} \frac{\pi r}{2R} & \text{for } r \leq R \\ \frac{\pi}{2} & \text{for } r > R, \end{cases} \quad (\text{C1})$$

where the + (−) sign corresponds to a meron (antimeron) and *R* is the “(anti)meron radius,” representing the typical size of our texture. The angle ϕ is the in-plane azimuthal angle, whereas ξ is an additional phase angle that determines the overall chirality. The dipolar interaction will only be considered as a contribution to the anisotropy, so energy terms of the form in Eq. (A3) will not appear explicitly in the analytical calculations below. As all the calculations herein will be for the above-Morin state with an easy-plane anisotropy ($K_{\text{eff}} < 0$), we will drop the “−” sign in Eq. (A2) above, and the absolute value $|K_{\text{eff}}|$ will be used throughout and designated as *K* for simplicity.

1. Analytical meron

We start by studying a linear meron, which is an extension of a calculation we have done previously [23,52], but with an iDMI term now included. We showed in Refs. [23,52] that the

exchange and anisotropy energy terms are independent of any phase angle ξ . This is not the case for the iDMI energy, which contains a term that explicitly depends on ξ . Using Eq. (A4), the resulting integral is

$$E_{\text{DMI}} = -Dt \cos \xi \iint \left(\frac{\pi r}{2R} + \cos \theta \sin \theta \right) dr d\phi. \quad (\text{C2})$$

As the first term comes from $\partial\theta/\partial r$, it is only nonzero for $r \leq R$. Moreover, it can be easily seen that for $r > R$, $\theta = \pi/2$ and hence $\cos \theta = 0$, so we only need to integrate the above expression in the range $0 < r \leq R$. Due to the axial symmetry, the integrand is independent of ϕ ; hence the angular integral results in a factor of 2π . Performing the radial integral gives

$$E_{\text{DMI}} = -\frac{1}{2}DRt \cos \xi (\pi^2 + 4). \quad (\text{C3})$$

The exchange and anisotropy energies from our previous calculations [23] are

$$E_{\text{Ex}} = 2\pi ANt \left[C + \ln \left(\frac{R_d}{R} \right) \right], \quad (\text{C4})$$

$$E_{\text{An}} = \frac{\pi^2 - 4}{2\pi} KNtR^2, \quad (\text{C5})$$

where $C \approx 2$ is a numerical constant that results from one of the integrals. Similar numerical integration constants appear throughout the equations presented here, and it should be understood that these are a consequence of the ansatz chosen, such that repeating these calculations with a different ansatz will result in a different constant. *N* is the number of AFM layers of thickness *t*, such that *Nt* is the total thickness of the film and *R_d* is a large length scale that is introduced to remove the infinite energy contribution from the whirling IP textures at large distances and will be discussed further in Sec. S1 of the Supplemental Material [41]. It is easy to see that *R_d* will not affect the energy minimization below, so it can later be set to infinity. We can then combine Eqs. (C3)–(C5) to get the total energy of an analytical linear meron

$$E_T = 2\pi ANt \left[C - \ln \left(\frac{R}{R_d} \right) \right] + \frac{\pi^2 - 4}{2\pi} KNtR^2 - \frac{1}{2}DRt \cos \xi (\pi^2 + 4). \quad (\text{C6})$$

As only the iDMI energy term has a chiral component (i.e., depends on ξ), if we minimize (C3) with respect to ξ , we can find the equilibrium chirality: $\xi = 2n\pi$ for integer *n* and positive *D* or $\xi = (2n + 1)\pi$ for negative *D*. We take $\xi = 0$ for convenience, which corresponds to a Néel meron of a fixed chirality and is an energy minimum under the assumption of a positive *D*, as is used in the simulations. One can also use the iDMI energy term to estimate the critical iDMI required to enforce homochirality by comparing with the thermal energy at room temperature. We see that $D_{\text{crit}}Rt(\pi^2 + 4) = 2k_B T$ and, accordingly, for the smallest observed texture radius and the value of *t* used throughout, $D_{\text{crit}} \approx 0.07$ mJ/m², i.e., D_{crit} is much smaller than the minimum value of iDMI otherwise considered here. We rescale the total energy by the film thickness and define an effective DMI strength $D_{\text{eff}} = D/N$. By minimizing the total energy with respect to *R* we can find the

equilibrium meron radius

$$R = \frac{\pi}{2K(\pi^2 - 4)} \left[\frac{1}{2} D_{\text{eff}}(\pi^2 + 4) \pm \sqrt{\frac{1}{4} D_{\text{eff}}^2(\pi^2 + 4)^2 + 8AK(\pi^2 - 4)} \right]. \quad (\text{C7})$$

In the limit of no iDMI or of thick films (such that $D_{\text{eff}} \rightarrow 0$), the result above reduces to that found previously in the absence of iDMI [23]. Furthermore, as all the terms in the square root are positive with our conventions, the “−” sign in the above expression would give a negative radius, which is unphysical and is therefore eliminated. As the z component of the normalized magnetization is given by $\cos(\pi r/2R)$, we find that $m_z = 0.5$ when $r = 2R/3$; hence comparing the meron radius R with the FWHM F , we obtain $F = 4R/3$.

To compare our results with previous analytical studies, e.g., Ref. [42], we introduce the characteristic length scale l_w and a dimensionless parameter κ defined as

$$l_w = \pi \sqrt{\frac{2A}{(\pi^2 - 4)K}} = \eta \sqrt{\frac{A}{K}},$$

$$\kappa = \frac{(\pi^2 + 4)}{[4\sqrt{2(\pi^2 - 4)}]} \frac{D_{\text{eff}}}{\sqrt{AK}} = \kappa_0 \frac{D_{\text{eff}}}{\sqrt{AK}}. \quad (\text{C8})$$

l_w is equivalent to the meron radius when $D_{\text{eff}} \rightarrow 0$, and κ is the unique dimensionless parameter that can be formed given the parameters involved, up to numerical factors (see Sec. VII). This allows us to express the meron radius in a simplified form

$$R = l_w(\kappa + \sqrt{\kappa^2 + 1}). \quad (\text{C9})$$

2. Other key analytical equations

Here, we present a brief description of the other equations relevant to this work, particularly for the scaling comparisons in Figs. 7(a) and 7(b). Firstly, the derivation of the linear antimeron largely follows the above and is given in full in Sec. S1 of the Supplemental Material [41]. The key difference with this derivation and that of the linear meron is the loss of circular symmetry in the presence of an iDMI; this leads to the introduction of an additional parameter λ that describes this distortion and can be determined by minimizing the energy in a similar way to the antimeron radius. The resulting coupled equations in terms of the parameters

l_w and κ are

$$R = l_w \left[\frac{1}{2} \kappa \left(\lambda - \frac{1}{\lambda} \right) + \sqrt{\frac{1}{4} \kappa^2 \left(\lambda - \frac{1}{\lambda} \right)^2 + \frac{1}{2} \left(\lambda^2 + \frac{1}{\lambda^2} \right)} \right], \quad (\text{C10})$$

$$\lambda = \frac{\kappa R}{2l_w [C + \ln(\frac{R_d}{R})]} + \sqrt{1 + \left\{ \frac{\kappa R}{2l_w [C + \ln(\frac{R_d}{R})]} \right\}^2}. \quad (\text{C11})$$

The distorted linear bimeron, as a first-order analytical approximation to the scaling behavior of a bimeron, is shown by the red line in Fig. 7(b). Clearly, this gives a reasonable prediction of the texture scales for the parameter values considered here but falls off rapidly both at larger and smaller κ . Critically, this simple model predicts that bimerons should be stable with significantly weaker iDMI than the lower bound we show here, and this is largely a failure of the continuum approximation used in the analytical calculations as the texture sizes tend towards the atomic scale where the discrete nature of the crystal will become critical. This is discussed further in Sec. S2 of the Supplemental Material [41]. The relevant coupled equations, which were solved iteratively to give the line discussed above, are

$$R = \frac{\pi \lambda D_{\text{eff}}}{K} \propto l_w \kappa \lambda, \quad (\text{C12})$$

$$0 = A\gamma \left(2\lambda - \frac{2}{\lambda^3} \right) - \frac{1}{2} \pi D_{\text{eff}} R. \quad (\text{C13})$$

The two skyrmion models that are used to compare with our simulation data, namely, the Walker ansatz [43] and the model presented by Büttner *et al.* [42], have the following equations, respectively, describing their radius as a function of the same phenomenological parameters we have used throughout.

$$R/l_w = \pi D \sqrt{\frac{A}{16AK^2 - \pi^2 DK^2}}, \quad (\text{C14})$$

$$R/l_w = \epsilon \kappa' \rho \frac{I_D(\rho)}{I_K(\rho)}. \quad (\text{C15})$$

Here, $\epsilon \approx 0.272$ is a numerical constant, ρ is a parameter that depends on κ' and l_w and controls the skyrmion profile, and I_D and I_K are functions of this parameter. R is implicitly defined in the second equation, since ρ itself depends on R . Therefore in order to plot the associated curve in Fig. 7(b), we solved this equation iteratively for many sets of values of the parameters κ' and l_w .

- [1] C. Back, V. Cros, H. Ebert, K. Everschor-Sitte, A. Fert, M. Garst, T. Ma, S. Mankovsky, T. L. Monchesky, M. Mostovoy, N. Nagaosa, S. S. P. Parkin, C. Pfleiderer, N. Reyren, A. Rosch, Y. Taguchi, Y. Tokura, K. von Bergmann, and J. Zang, The 2020 skyrmionics roadmap, *J. Phys. D: Appl. Phys.* **53**, 363001 (2020).
- [2] X. Zhang, Y. Zhou, K. M. Song, T.-E. Park, J. Xia, M. Ezawa, X. Liu, W. Zhao, G. Zhao, and S. Woo, Skyrmion-electronics: Writing, deleting, reading and processing magnetic skyrmions

toward spintronic applications, *J. Phys.: Condens. Matter* **32**, 143001 (2020).

- [3] Y. Tokura and N. Kanazawa, Magnetic skyrmion materials, *Chem. Rev. (Washington, DC)* **121**, 2857 (2020).
- [4] H. Bai, X. Zhou, Y. Zhou, X. Chen, Y. You, F. Pan, and C. Song, Functional antiferromagnets for potential applications on high-density storage and high frequency, *J. Appl. Phys. (Melville, NY)* **128**, 210901 (2020).

- [5] J. Barker and O. A. Tretiakov, Static and Dynamical Properties of Antiferromagnetic Skyrmions in the Presence of Applied Current and Temperature, *Phys. Rev. Lett.* **116**, 147203 (2016).
- [6] X. Zhang, Y. Zhou, and M. Ezawa, Antiferromagnetic skyrmion: Stability, creation and manipulation, *Sci. Rep.* **6**, 24795 (2016).
- [7] W. Legrand, D. Maccariello, F. Ajejas, S. Collin, A. Vecchiola, K. Bouzehouane, N. Reyren, V. Cros, and A. Fert, Room-temperature stabilization of antiferromagnetic skyrmions in synthetic antiferromagnets, *Nat. Mater.* **19**, 34 (2020).
- [8] X. Zhang, Y. Zhou, and M. Ezawa, Magnetic bilayer-skyrmions without skyrmion Hall effect, *Nat. Commun.* **7**, 10293 (2016).
- [9] T. Shiino, S.-H. Oh, P. M. Haney, S.-W. Lee, G. Go, B.-G. Park, and K.-J. Lee, Antiferromagnetic Domain Wall Motion Driven by Spin-Orbit Torques, *Phys. Rev. Lett.* **117**, 087203 (2016).
- [10] S. Rohart and A. Thiaville, Skyrmion confinement in ultrathin film nanostructures in the presence of Dzyaloshinskii-Moriya interaction, *Phys. Rev. B* **88**, 184422 (2013).
- [11] H. Yang, A. Thiaville, S. Rohart, A. Fert, and M. Chshiev, Anatomy of Dzyaloshinskii-Moriya Interaction at Co/Pt Interfaces, *Phys. Rev. Lett.* **115**, 267210 (2015).
- [12] R. Msiska, D. R. Rodrigues, J. Leliaert, and K. Everschor-Sitte, Nonzero Skyrmion Hall Effect in Topologically Trivial Structures, *Phys. Rev. Applied* **17**, 064015 (2022).
- [13] H. Velkov, O. Gomonay, M. Beens, G. Schwiete, A. Brataas, J. Sinova, and R. A. Duine, Phenomenology of current-induced skyrmion motion in antiferromagnets, *New J. Phys.* **18**, 075016 (2016).
- [14] L. Shen, J. Xia, X. Zhang, M. Ezawa, O. A. Tretiakov, X. Liu, G. Zhao, and Y. Zhou, Current-Induced Dynamics and Chaos of Antiferromagnetic Bimerons, *Phys. Rev. Lett.* **124**, 037202 (2020).
- [15] R. Lebrun, A. Ross, S. A. Bender, A. Qaiumzadeh, L. Baldrati, J. Cramer, A. Brataas, R. A. Duine, and M. Kläui, Electrically tunable long-distance transport in crystalline antiferromagnetic iron oxide, *Nature (London)* **561**, 222 (2018).
- [16] R. Lebrun, A. Ross, O. Gomonay, V. Baltz, U. Ebels, A.-L. Barra, A. Qaiumzadeh, A. Brataas, J. Sinova, and M. Kläui, Long-distance spin-transport across the Morin phase transition up to room temperature in ultra-low damping single crystals of the antiferromagnet α -Fe₂O₃, *Nat. Commun.* **11**, 6332 (2020).
- [17] R. Lebrun, A. Ross, O. Gomonay, S. A. Bender, L. Baldrati, F. Kronast, A. Qaiumzadeh, J. Sinova, A. Brataas, R. A. Duine, and M. Kläui, Anisotropies and magnetic phase transitions in insulating antiferromagnets determined by a spin-Hall magnetoresistance probe, *Commun. Phys.* **2**, 50 (2019).
- [18] J. Fischer, M. Althammer, N. Vlietstra, H. Huebl, S. T. B. Goennenwein, R. Gross, S. Geprägs, and M. Opel, Large Spin Hall Magnetoresistance in Antiferromagnetic α -Fe₂O₃/Pt Heterostructures, *Phys. Rev. Applied* **13**, 014019 (2020).
- [19] A. Ross, R. Lebrun, C. Ulloa, D. A. Grave, A. Kay, L. Baldrati, F. Kronast, S. Valencia, A. Rothschild, and M. Kläui, Structural sensitivity of the spin Hall magnetoresistance in antiferromagnetic thin films, *Phys. Rev. B* **102**, 094415 (2020).
- [20] Y. Cheng, S. Yu, M. Zhu, J. Hwang, and F. Yang, Electrical Switching of Tristate Antiferromagnetic Néel Order in α -Fe₂O₃ Epitaxial Films, *Phys. Rev. Lett.* **124**, 027202 (2020).
- [21] E. Cogulu, N. N. Statuto, Y. Cheng, F. Yang, R. V. Chopdekar, H. Ohldag, and A. D. Kent, Direct imaging of electrical switching of antiferromagnetic Néel order in α -Fe₂O₃ epitaxial films, *Phys. Rev. B* **103**, L100405 (2021).
- [22] F. P. Chmiel, N. Waterfield-Price, R. D. Johnson, A. D. Lamirand, J. Schad, G. van der Laan, D. T. Harris, J. Irwin, M. S. Rzechowski, C.-B. Eom, and P. G. Radaelli, Observation of magnetic vortex pairs at room temperature in a planar α -Fe₂O₃/Co heterostructure, *Nat. Mater.* **17**, 581 (2018).
- [23] H. Jani, J.-C. Lin, J. Chen, J. Harrison, F. Maccherozzi, J. Schad, S. Prakash, C.-B. Eom, A. Ariando, T. Venkatesan, and P. G. Radaelli, Antiferromagnetic half-skyrmions and bimerons at room temperature, *Nature (London)* **590**, 74 (2021).
- [24] T. W. B. Kibble, Topology of cosmic domains and strings, *J. Phys. A: Math. Gen.* **9**, 1387 (1976).
- [25] W. H. Zurek, Cosmological experiments in superfluid helium?, *Nature (London)* **317**, 505 (1985).
- [26] A. del Campo and W. H. Zurek, Universality of phase transition dynamics: topological defects from symmetry breaking, *Int. J. Mod. Phys. A* **29**, 1430018 (2014).
- [27] J. M. D. Coey, *Magnetism and Magnetic Materials* (Cambridge University Press, Cambridge, 2009), pp. 418–420.
- [28] C. Shull, W. Strauser, and E. Wollan, Neutron diffraction by paramagnetic and antiferromagnetic substances, *Phys. Rev.* **83**, 333 (1951).
- [29] F. J. Morin, Magnetic susceptibility of α -Fe₂O₃ and α -Fe₂O₃ with added titanium, *Phys. Rev.* **78**, 819 (1950).
- [30] A. H. Morrish, *Canted Antiferromagnetism: Hematite* (World Scientific, Singapore, 1994).
- [31] P. J. Besser, A. H. Morrish, and C. W. Searle, Magnetocrystalline anisotropy of pure and doped hematite, *Phys. Rev.* **153**, 632 (1967).
- [32] J. O. Artman, J. C. Murphy, and S. Foner, Magnetic anisotropy in antiferromagnetic corundum-type sesquioxides, *Phys. Rev.* **138**, A912 (1965).
- [33] H. Jani, J. Linghu, S. Hooda, R. V. Chopdekar, C. Li, G. J. Omar, S. Prakash, Y. Du, P. Yang, A. Banas, K. Banas, S. Ghosh, S. Ojha, G. R. Umapathy, D. Kanjilal, A. Ariando, S. J. Pennycook, E. Arenholz, P. G. Radaelli, J. M. D. Coey, Y. P. Feng, and T. Venkatesan, Reversible hydrogen control of antiferromagnetic anisotropy in α -Fe₂O₃, *Nat. Commun.* **12**, 1668 (2021).
- [34] A. Vansteenkiste, J. Leliaert, M. Dvornik, M. Helsen, F. Garcia-Sanchez, and B. Van Waeyenberge, The design and verification of MuMax3, *AIP Adv.* **4**, 107133 (2014).
- [35] J. De Clercq, J. Leliaert, and B. Van Waeyenberge, Modelling compensated antiferromagnetic interfaces with MuMax3, *J. Phys. D: Appl. Phys.* **50**, 425002 (2017).
- [36] D. Suess, T. Schrefl, W. Scholz, J.-V. Kim, R. L. Stamps, and J. Fidler, Micromagnetic simulation of antiferromagnetic/ferromagnetic structures, *IEEE Trans. Magn.* **38**, 2397 (2002).
- [37] V. V. Mazurenko and V. I. Anisimov, Weak ferromagnetism in antiferromagnets: α -Fe₂O₃ and La₂CuO₄, *Phys. Rev. B* **71**, 184434 (2005).
- [38] L. Exl, S. Bance, F. Reichel, T. Schrefl, H. P. Stimming, and N. J. Mauser, Labonte's method revisited: An effective steepest descent method for micromagnetic energy minimization, *J. Appl. Phys. (Melville, NY)* **115**, 17D118 (2014).
- [39] J. Mulkers, B. Van Waeyenberge, and M. V. Milošević, Effects of spatially-engineered Dzyaloshinskii-Moriya interaction in ferromagnetic films, *Phys. Rev. B* **95**, 144401 (2017).

- [40] A. Aharoni, *Introduction to the Theory of Ferromagnetism* (Oxford University Press, Oxford, 1996).
- [41] See Supplemental Material at <http://link.aps.org/supplemental/10.1103/PhysRevB.105.224424> for further derivations of analytical equations and additional simulation data.
- [42] F. Büttner, I. Limesh, and G. S. D. Beach, Theory of isolated magnetic skyrmions: From fundamentals to room temperature applications, *Sci. Rep.* **8**, 4464 (2018).
- [43] X. S. Wang, H. Y. Yuan, and X. R. Wang, A theory on skyrmion size, *Commun. Phys.* **1**, 31 (2018).
- [44] M. Hoffmann, G. P. Müller, and S. Blügel, Atomistic Perspective of Long Lifetimes of Small Skyrmions at Room Temperature, *Phys. Rev. Lett.* **124**, 247201 (2020).
- [45] N. Gao, S.-G. Je, M.-Y. Im, J. W. Choi, M. Yang, Q. Li, T. Y. Wang, S. Lee, H.-S. Han, K.-S. Lee, W. Chao, C. Hwang, J. Li, and Z. Q. Qiu, Creation and annihilation of topological merons in in-plane magnetized films, *Nat. Commun.* **10**, 5603 (2019).
- [46] E. G. Galkina, A. Y. Galkin, B. A. Ivanov, and F. Nori, Magnetic vortex as a ground state for micron-scale antiferromagnetic samples, *Phys. Rev. B* **81**, 184413 (2010).
- [47] M. Augustin, S. Jenkins, R. F. L. Evans, K. S. Novoselov, and E. J. G. Santos, Properties and dynamics of meron topological spin textures in the two-dimensional magnet CrCl_3 , *Nat. Commun.* **12**, 185 (2021).
- [48] B. Göbel, A. Mook, J. Henk, I. Mertig, and O. A. Tretiakov, Magnetic bimerons as skyrmion analogues in in-plane magnets, *Phys. Rev. B* **99**, 060407(R) (2019).
- [49] A. O. Leonov and I. Kézsmárki, Asymmetric isolated skyrmions in polar magnets with easy-plane anisotropy, *Phys. Rev. B* **96**, 014423 (2017).
- [50] A. S. Araújo, R. J. C. Lopes, V. L. Carvalho-Santos, A. R. Pereira, R. L. Silva, R. C. Silva, and D. Altbir, Typical skyrmions versus bimerons: A long-distance competition in ferromagnetic racetracks, *Phys. Rev. B* **102**, 104409 (2020).
- [51] R. L. Silvia, Antiferromagnetic-bimeron dynamics driven by a spin-polarized current at an inhomogeneous racetrack, *Phys. Lett. A* **403**, 127399 (2021).
- [52] P. G. Radaelli, J. Radaelli, N. Waterfield-Price, and R. D. Johnson, Micromagnetic modeling and imaging of vortex | meron structures in an oxide | metal heterostructure, *Phys. Rev. B* **101**, 144420 (2020).
- [53] L. Cai, E. M. Chudnovsky, and D. A. Garanin, Collapse of skyrmions in two-dimensional ferromagnets and antiferromagnets, *Phys. Rev. B* **86**, 024429 (2012).
- [54] A. De Lucia, K. Litzius, B. Krüger, O. A. Tretiakov, and M. Kläui, Multiscale simulations of topological transformations in magnetic-skyrmion spin structures, *Phys. Rev. B* **96**, 020405(R) (2017).
- [55] E. J. Samuelsen and G. Shirane, Inelastic neutron scattering investigation of spin waves and magnetic interactions in $\alpha\text{-Fe}_2\text{O}_3$, *Phys. Status Solidi B* **42**, 241 (1970).
- [56] J. M. D. Coey and G. A. Sawatzky, A study of hyperfine interactions in the system $(\text{Fe}_{1-x}\text{Rh}_x)_2\text{O}_3$ using the Mössbauer effect, *J. Phys. C: Solid State Phys.* **4**, 2386 (1971).
- [57] S. Park, H. Jang, J.-Y. Kim, B.-G. Park, T.-Y. Koo, and J.-H. Park, Strain control of Morin temperature in epitaxial $\alpha\text{-Fe}_2\text{O}_3(0001)$ film, *Europhys. Lett.* **103**, 27007 (2013).
- [58] A. Cao, R. Chen, X. Wang, X. Zhang, S. Lu, S. Yan, B. Koopmans, and W. Zhao, Enhanced interfacial Dzyaloshinskii-Moriya interactions in annealed Pt/Co/MgO structures, *Nanotechnology* **31**, 155705 (2020).